Advanced Steel Construction – Vol. 22 No. 1 (2026) 78–95
DOI:10.18057/IJASC.2026.22.1.7

STUDY ON DYNAMIC PERFORMANCE OF STEEL-WOOD COMPOSITE BEAM-COLUMN JOINTS UNDER IMPACT LOAD

Chang Wu [1, 2], Ying-Ni Fan [1, *], Yue-Han Zhang [1] and Yu-Tong Tian [1]

[1] *School of Civil Engineering, Lanzhou University of Technology, Lanzhou 730050, China*
[2] *Western Center of Disaster Mitigation in Civil Engineering of Ministry of Education, Lanzhou University of Technology, Lanzhou 730050, China*
** (Corresponding author: E-mail: 3121825025@qq.com)*

ABSTRACT

This paper proposes a novel steel-timber hybrid beam-column joint suitable for the "timber above and steel below" low-rise hybrid structural system. Sleeves and L-shaped connectors are set up at the joints. Sleeves are set up to prevent the wood from cracking, while L-shaped connectors prevent the steel column from twisting when connecting the upper wood column to the lower I-beam. In order to investigate the impact resistance, the deformation characteristics, damage mechanism and energy dissipation capacity were investigated through tests and numerical simulations. The effects of key parameters such as impact mass, velocity, position, impactor shape, and beam end constraints on the impact resistance of the joints were also analyzed. The results show that the joint's performance overall was excellent, in which the L-shaped connector served as the primary deformation zone. The joint's deformation and displacement under the same impact conditions were reduced significantly by reinforcing the connector's thickness. Furthermore, the spring support replaced the crossbeam's restraint function effectively during the tests. The parametric analysis revealed that an increase in the hammer's velocity at impact leads directly to a significant increase in the impact's peak force and a prolonged impact platform. In contrast, an increase in the hammer's mass had a limited effect on the impact's peak force, and merely extended its decay process. Based upon the experimental results and parametric analysis, the vulnerabilities of the steel-timber hybrid joint in the "timber above and steel below" structural system were identified, and corresponding improvement measures are proposed.

ARTICLE HISTORY

Received: 18 January 2025
Revised: 14 June 2025
Accepted: 15 June 2025

KEYWORDS

Steel-timber hybrid structure;
Beam-column node;
Impact test;
Dynamic properties;
Damage mechanism

1. Introduction

With the growing demand for green, low-carbon and sustainable building structures, assembled structures are gradually becoming a hot research topic in the engineering field. However, impact events occur in people's daily lives in a wide range, from a simple cup of water falling from a high shelf to a space shuttle colliding with a meteor [1]. This paper synthesizes the characteristics of residential houses in Northwest China, and proposes an "timber above and steel below" structure. Due to the large difference in material properties between steel and wood, the joint connections have complex stresses, so it is innovative to design a steel-wood combined connection joint, and focus on its dynamic response under the action of impact loading. Many scholars have conducted relevant research on hybrid structures. While the research on hybrid structures mainly focuses on the combination of steel with concrete, aluminum alloy and other materials, and mainly discusses their seismic performance [2-5], A lot of research has also been done on the mechanical properties of structures under impact loading, Zhang et al. [6] conducted numerical evaluations using LS-DYNA to assess the nonlinear dynamic response and failure behavior of supported reinforced concrete (RC) beams subjected to impact and blast loads. Damian et al. [7-8] developed detailed nonlinear three-dimensional finite element models (FEMs) using ABAQUS and conducted rigorous validations to ensure consistency between the model and published experimental tests with respect to force and displacement time histories. Ja'e et al. [9] investigated the structural impact resistance of lightweight fiber reinforced concrete. Zeng et al. [10-11] investigated the dynamic response of reinforced concrete (SRC) composite members under transverse impact through experiments and numerical simulations. Zhu et al. [12] researched cruciform steel-reinforced concrete-filled steel tubes' impact performance under lateral impact loads. Kang et al. [13] investigated the dynamic response of steel-tube concrete beams in the peak phase under lateral impact, Huang et al. [14-19] investigated the mechanical properties, dynamic response and computational methods of steel, concrete and composite beams under impact by means of experiments and numerical simulations.

Furthermore, Yang et al. [20-21] investigated the mechanical properties of steel-wood composite beams and composite joints through tests and finite element analysis. Kia et al.[22] conducted an experimental study on the bearing capacity, failure mechanisms, stiffness, and ductility of 48 hybrid members with wrapped steel bars adhered within wooden sleeves under concentric axial compression, and compared them with bare wooden columns. Chen et al. [23-27] proposed a variety of new types of beam-column steel-timber connection joints and investigated the damage modes and mechanical properties of the new types of joints under cyclic loading through tests and finite elements. Dourado et al. [28] investigated steel-timber joints' fracture behavior under quasi-static loading, and Zheng et al. [29] discussed the importance of connections between concrete-filled steel tubular columns and composite beams for structural resistance to floor-by-floor collapse. Moreover, through experimental and numerical studies, they compared three different types of connections and two types of shear connectors, and explored their failure modes, vertical resistance-deformation mechanisms, and strain-deformation relations.

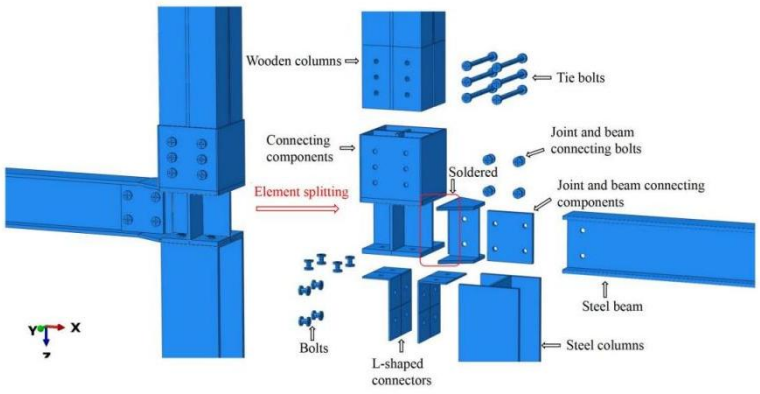

Fig. 1 Schematic diagram of joint construction

In summary, the existing research on composite structures mainly focuses on steel-mixed and steel-aluminum structures, and the research on structural performance under dynamic loading mainly focuses on reinforced concrete structures, while the research on steel-wood composite structures is limited to static research, especially in the research on the dynamic response of steel-wood structures under impact loading is still lacking, especially in the failure mechanism of steel-wood composite members under dynamic loading, which is yet to be studied in depth and detail. In particular, the failure mechanism of steel-wood composite members under dynamic loading is still in need of in-depth and detailed research.

This paper proposes a novel hybrid steel-timber beam-column joint, cut cross groove in the middle of the wooden post, and fix and connect the cross connecting key with the wooden post through tie bolts; at the same time, set a circle of sleeve on the periphery of the cross connecting key to prevent the wood from cracking. A connecting plate is set at the bottom of the cross connecting key, and the connection between the lower I-beam and the cross connecting key is realized through L-shaped connectors and bolts; a trapezoidal connecting key is welded to the side of the cross connecting key, and the steel beam is connected to the cross connecting key through bolts and connecting plate, as shown in Fig. 1. Through experimental research and numerical simulation, the deformation mode, damage mechanism and energy consumption capacity of steel-wood hybrid beam-column nodes are investigated, and the key parameters are analyzed to investigate the effects of different impact conditions on the impact resistance of steel-wood hybrid beam-column joint.

2. Douglas fir lumber material property tests

The moisture content of the Douglas fir timber used was measured according to the “Method for the Determination of the Moisture Content of Wood” (GB/T 1931-2009) [30]. Through measurement and calculation analysis, it was found that the Douglas fir timber’s average moisture content was 10.79%, which complies with the value (9% to 12%) in relevant specifications.

The load-displacement curve of wood along the grain was measured according to the “Test Method for Compression Strength Parallel to Grain of Wood” (GB/T 1935-2009) [31], as shown in Fig. 2.

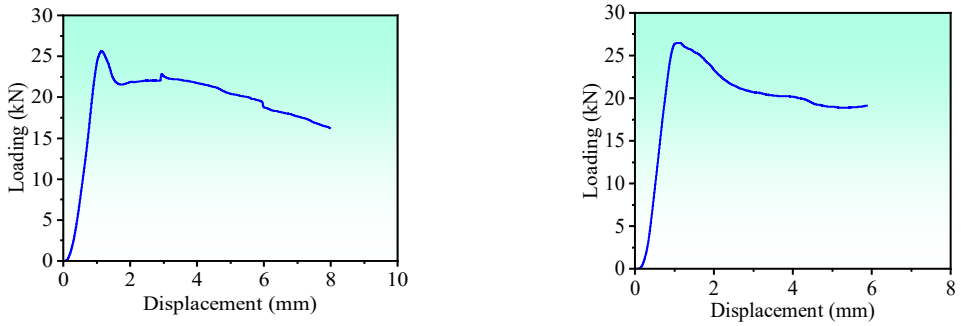

(a) Specimen I (b) Specimen II

Fig. 2 Compression resistance curve of wood with parallel grain

According to the data in the figure, the minimum compressive load-bearing capacity of Douglas fir wood along the grain is 21.04 kN, the maximum is 27.54 kN, and the average is 24.51 kN. The minimum compressive strength is 52.10 MPa, the maximum is 67.69 MPa, and the mean is 60.95 MPa. The mean compressive strength along the grain when the specimen’s moisture content is 12% is 56.97 MPa.

The specimen’s tensile strength was measured by the relevant provisions of the “Test Method for Tensile Strength Parallel to Grain of Wood” (GB/T 1938-2009) [32], and the test process is shown in Fig. 3.

Fig. 3 Tensile strength test of wood along the grain

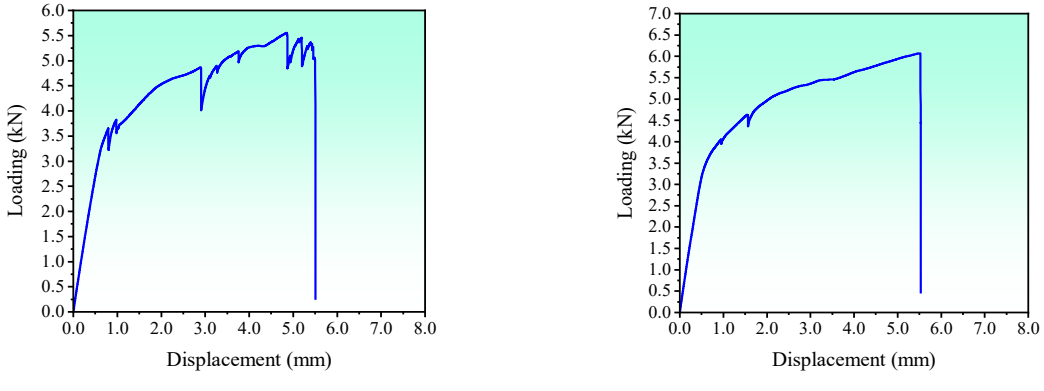

(a) Specimen I (b) Specimen II

Fig. 4 Tensile curve diagram of wood along the grain

According to the data in Fig. 4, Douglas fir wood's minimum tensile load-bearing capacity is 4.96 kN, the maximum is 5.85 kN, and the mean is 4.96 kN. The minimum tensile strength is 79.52 MPa, the maximum is 95.88 MPa, and the mean is 86.67 MPa. When the specimen's moisture content is 12%, the mean tensile strength along the grain is 84.93 MPa.

The mean value of the reduction coefficients of the wood's grain-longitudinal tensile strength, flexural strength, and compressive strength, which is (0.80+0.446+0.567)/3=0.6, was used to reduce the wood properties. The reduction coefficients for different influencing factors are shown in Table 1, and the material property test results on the reduced wood are detailed in Table 2.

Table 1
Discount factors for different impact factors

Stress state of wood	Parallel grain tensile strength	Compressive strength of smooth grain	Bending strength
Effects of natural wood defects K_{Q1}	0.80	0.66	0.75
Effects of wood drying defects K_{Q2}	——	0.90	0.85
Long-term load strength effects K_{Q3}	1.0	1.0	1.0
Wood size effects K_{Q4}	——	0.75	0.89
Discount factor K_Q	0.80	0.446	0.567

Note: Since the wood used in this test was new and not subjected to long-term loading, the factor K_{Q3} for this item is 1.0;

Table 2
Adjustment results of wood material performance tests

Norm	Moisture content%	Flexural modulus of elasticity （MPa）	Bending strength （MPa）	Compressive strength of smooth grain （MPa）	Parallel grain tensile strength （MPa）
Average value	10.79	10290	36.08	34.18	50.96

3. Steel-wood hybrid beam-column node drop hammer impact test

3.1. Joint location selection

This experiment used Q235 steel with an elastic modulus of $E = 2.06 \times 10^5$ MPa, in which Douglas fir's measured elastic modulus is $E = 10290$MPa. The construction form of the middle-layer, middle-column joint was taken as the research object (as illustrated in Fig. 5). Because the upper column in the "upper wood and lower steel" system is a wooden column, the difference in material properties leads to different lateral stiffness. Therefore, under the condition of constant boundary constraints, it is necessary to calculate the column length for the simplified model of the joint.

The moment of inertia is calculated according to eq. (1):

$$I = \frac{bh^3}{12} = \frac{200^4}{12} = 133333333mm^4 \quad (1)$$

The steel columns are H-beam columns and their moment of inertia is calculated according to eq. (2):

$$I = \frac{BH^3 - bh^3}{12} = 46104900mm^4 \quad (2)$$

Where: B-bottom width;
H -- the height of the I-beam;
h -- the internal height of the I-beam;
b -- the 1/2 bottom width;

The length ratio of steel columns to wood columns is calculated according to eq. (3) while ensuring that the columns' bending stiffness overall was the same.

$$\frac{L_{steel}}{L_{numb}} = \frac{E_{steel}I_{steel}}{E_{numb}I_{numb}} = \frac{2.06\times10^5\times46104900}{10290\times133333333} = 1.41 \quad (3)$$

Here, an approximate value of 1.5 was taken, such that the steel column was 1.5m and the wooden column was 1m.

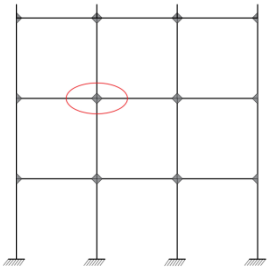

Fig. 5 Simplified model of node structure

3.2. Specimen design

In order to investigate the effects of impact location, sleeve thickness and L-shaped connector thickness on the impact resistance of steel-wood composite beam-column joints. In this paper, this experiment conducted drop hammer impact tests on six steel-wood hybrid columns, with three impacts on the steel column's mid-span, two on the joint location, and one on the wooden column's mid-span. Among them, the design specimens, M-SWMC-S-1-3 and M-SWMC-J-1-2, are intended to investigate the effect of the thickness of the sleeve and L-shaped connector on the impact resistance of the joint, while M-SWMC-S-1, M-SWMC-J-2, and M-SWMC-W are used to investigate the most unfavorable position of the structure under the same impact conditions. Considering that during lateral impact, the beam in the direction of the impact provides support to the joint, and in the actual frame, this beam is semi-rigid, the remote end of the joint does not restrict the entire beam's lateral displacement. Therefore, to determine the column member's dynamic response when subjected to impact load alone, this experiment used semi-rigid spring supports to replace the beams to provide reaction force, This support combines the characteristics of a rigid and flexible support by means of elastic deformation of the spring element and a damping mechanism that provides limited rotational or translational restraint while also absorbing and transferring loads, as shown in Fig. 6. The maximum constant load it can withstand is 500kN, with a maximum allowable vertical displacement of 200mm. The main parameters considered in the experiment were the hammer's mass (M), its velocity (V), and the impact location. In this design, the specimen size is selected according to the principle of simplified modeling in section 2.1 of the text to select the length of the member, and its cross-section dimensions refer to the "Code for the Design of Steel Structures" and the "Manual for the Design of Wooden Structures" [33] [34] design the joint. At the joint, the steel column designed is an H-shaped steel 200mm×200mm×8mm×12mm and a length of 1500mm. The wooden column has a cross-sectional dimension of 200mm×200mm and a length of 1000mm. The sleeves at the joints and L-shaped connectors are all constructed by welding, including three 5mm sleeves and three 10mm sleeves, eight 6mm L-shaped connectors, and four 10mm L-shaped connectors. The specimens' geometric parameters are detailed in Table 3, and the physical diagrams of each part of the components are shown in Fig. 7.

Naming Explanation: In "M-SWMC-S", "M" stands for "Middle", referring to the middle joint of the column; "SWMC" is the abbreviation for "Steel-wood Mixed Columns"; "S" represents that the impact location is at the mid-span of the steel column, "J" indicates that the impact location is at the joint, and "W" signifies that the impact location is at the mid-span of the wooden column.

Fig. 6 Physical drawing of spring support

Table 3
Geometric parameters of test pieces

Serial number	Specimen number	Impact position	Section size（mm）	Joint's sleeve thickness（mm）	Thickness of L-shaped connector（mm）
1	M-SWMC-S-1	Steel column span center	200×200	5	6
2	M-SWMC-S-2	Steel column span center	200×200	10	6
3	M-SWMC-S-3	Steel column span center	200×200	5	10
4	M-SWMC-J-1	Nodal	200×200	10	10
5	M-SWMC-J-2	Nodal	200×200	10	6
6	M-SWMC-W	center of Wooden pole spanning	200×200	5	6

(a) Overall diagram of unassembled components (b) Groove and hole cutting diagram of wooden column (c) Sleeve for joint without cross-piece

Fig. 7 Detailed drawing of test component elements

3.3. Measurement program

The core measurements in this experimental test included the specimen's vertical displacement (at the joint, the steel column's mid-span, and the wooden column's mid-span), acceleration (at the joint, the steel column's mid-span, and the wooden column's mid-span), as well as the L-shaped connectors' strain and the strain on the opposite side of the impact location on the steel and wooden columns. The joint's vertical displacement and the column's deflection at the mid-span were measured directly using dynamic displacement meters, while the strain was measured through strain gauges. Detailed measurement point layouts are shown in Figs. 8, 9, and 10.

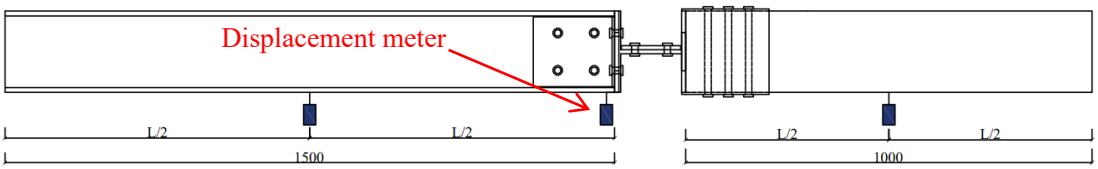

Fig. 8 Displacement meter layout

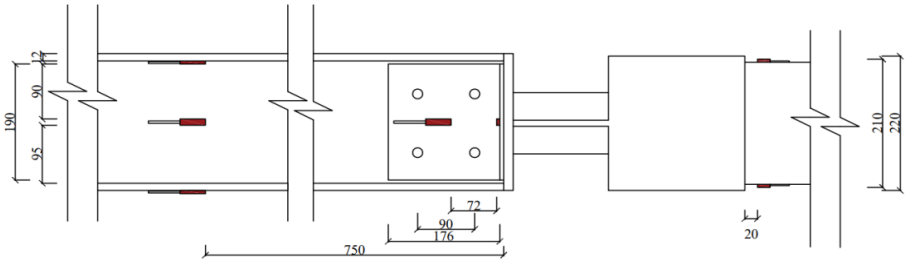

Fig. 9 Specimen strain gauge layout

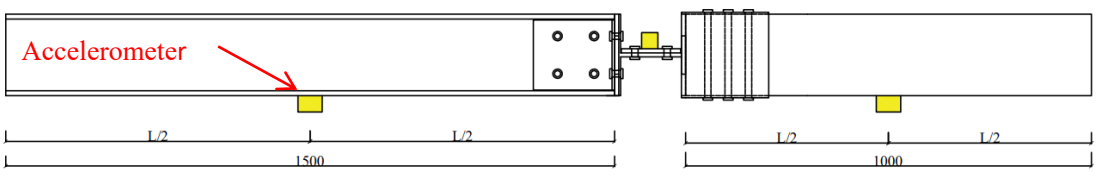

Fig. 10 Accelerometer arrangement

3.4. Impact test device set-up

The drop hammer impact test for the joints in this study was conducted on a large platform with a maximum lifting height of 18 meters and a maximum impact energy of 330,000 joules. Equipped with a high-precision dynamic data testing system, a high-speed camera (to record the joints' failure and deformation process), and a safety control system, this platform meets the experimental requirements fully. Figs. 11 and 12 show the experimental apparatus's schematic diagrams.

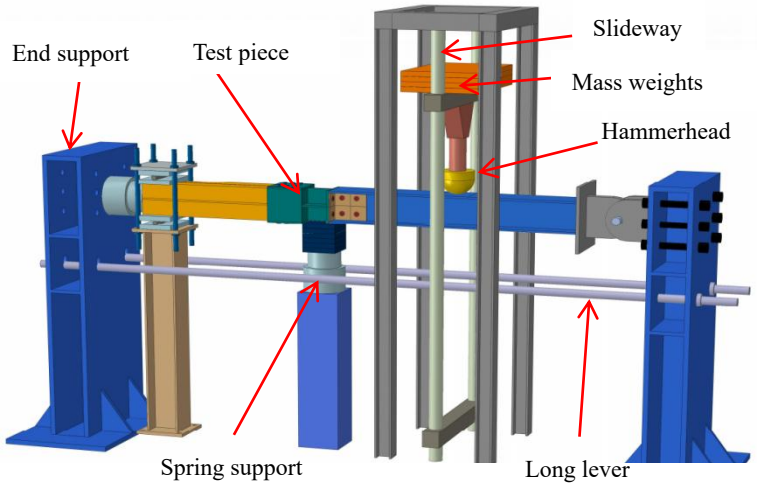

Fig. 11 Sketch of the test setup

Fig.12 Front of test loading device

This test takes falling stone impact as the research background, and the impact location is the middle of the steel column span, at the joint, and the middle of the wooden column span, respectively. Considering that the size of falling stone impact energy is mainly determined by the impact velocity and falling stone mass, therefore, referring to the research of Gao et. al [35] and combining with the impact height of the impact test platform of the falling hammer impact test platform and the mass of the falling hammer, the impact test parameters in Table 4 are designed. To simulate different experimental parameters' influence on the steel-wood mixed column joints' dynamic performance under drop hammer impact, controlled experiments were designed with varying drop hammer speeds, impact times, and impact locations, with a total of six specimens for steel-wood hybrid columns.

Table 4
Table of impact test parameters for steel-wood hybrid column nodes

Specimen number	Impact mass M	Impact velocity V	Impact energy EK(kJ)	Impact Height H（m）	Number of impacts
		3.16	1.60	0.5	
M-SWMC-S-1	320	4.47	3.20	1	3
		6.32	6.39	2	
		3.16	1.60	0.5	
M-SWMC-S-2	320	4.47	3.20	1	3
		6.32	6.39	2	
	320		6.39		
M-SWMC-S-3	420	6.32	8.39	2	3
	500		9.99		
		3.16	1.60	0.5	
M-SWMC-J-1	320	4.47	3.20	1	3
		5.48	4.80	1.5	
		3.16	1.60	0.5	
M-SWMC-J-2	320	4.47	3.20	1	3
		5.48	4.80	1.5	
		3.16	1.60	0.5	
M-SWMC-W	320	4.47	3.20	1	3
		5.48	4.80	1.5	

During the experiment, the drop hammer system's force sensor and dynamic displacement sensor, respectively, recorded the time history curves of the impact's force and vertical displacement of the impact point precisely. The impact process for the M-SWMC-S-2 specimen can be divided into three main stages through the time history curve: peak, stability, and attenuation. Specifically, this process is subdivided into eight stages: non-contact; initial contact; common downward movement; maximum displacement; rebound upward; imminent separation; rebound separation; and oscillation and stillness. Part of the process is shown in Fig. 13.

(a) The head is not in contact with the specimen

(b) Initial contact between the hammer head and the specimen

(c) The oscillation of the specimen tends to be static

Fig. 13 Diagram of partial impact process

3.5. Test loading process

Figs. 14-15, respectively, show the deformation mode and local deformation of specimens M-SWMC-S-1 and M-SWMC-S-2 in this impact test overall, which analyzed multiple impacts' influence on the deformation of different components of the specimens under the same impact energy. Comparing the two specimens, the structural deformation is mainly concentrated in the bending at the joints and the tensile deformation of the L-shaped connector; the plastic hinge is first formed in the tensile region of the L-shaped connectors, and gradually extends to the beam section in the core area of the joint, and to the connection between the wooden columns and the steel sleeve. These deformations increased as the height of each impact gradually increased. Especially after the third impact, the deformation of the L-connector reached a serious level, which led to a change in the relative position between the H-shaped beam column and the bottom plate of the joint's sleeve, and eventually led to the separation of the two. Although the specimen M-SWMC-S-2 was strengthened in the thickness of the sleeve, it did not have a significant effect on the overall deformation of the member, and the displacement difference between the L-shaped connector and the bottom plate of the sleeve still increased with the increase in the number of impacts, indicating that the strengthening of the sleeve thickness has a limited effect on the improvement of the fatigue performance of the connector.

As there was no change in the first two specimens' hammer mass, Therefore, the test was carried out on specimen M-SWMC-S-3 with the thickness of the reinforced L- shaped connector. As can be seen in Fig. 16, compared to specimen M-SWMC-S-1, specimen M-SWMC-S-3's deformation overall was smaller

than that of the first two specimens. After the third impact, M-SWMC-S-3 showed significant changes, the column tilted as a whole, the bolts connecting the L-shaped connector to the joint base plate tilted, and plastic hinges were first formed at the connection between the L-shaped connector and the bolts and expanded to the periphery with the increase of the number of impacts; the L-shaped connector appeared to be slightly bent on the opposite side of the impacts, and plastic hinges were formed in the bending place, which led to the concentration of the stresses. Wood post cracks extend radially in the direction of the wood fibers; two vertical cracks appeared along the joint cross-member at the slotted end of the wood column, and the cracks extended from the slotted edge to the center of the column. Despite the multiple damage to M-SWMC-S-3, with the strengthened L- shaped connector, its impact resistance is still significantly higher than that of M-SWMC-S-1, highlighting the critical role of the strength of the L-shaped connector on the impact resistance of the joint.

Next, the location where the joint sustained impact was changed to investigate its influence on the components' overall and dynamic performance. By comparing the deformation of joints M-SWMC-J-1 and M-SWMC-J-2 with L-shaped connectors of different thicknesses under the same hammer mass and velocity, From Fig. 17 and Fig. 18, it can be seen that under the impact of the two joints, the impact side of the L-shaped connector is deformed in tension and bending, and the plastic hinge is formed and expanded firstly here, and at the same time, the joint base plate and the H-beam column are displaced vertically relative to each other. Due to the different thicknesses of the L-shaped connectors, the overall deformation of M-SWMC-J-1 is obviously smaller than that of M-SWMC-J-2, and the displacement between the node base plate and the H-shaped steel column is also smaller. Comparing specimens M-SWMC-J-1 and M-SWMC-J-2, because of the L-shaped connectors' reinforcement, specimen M-SWMC-J-1's deformation was significantly less than that of specimen M-SWMC-J-2. Further, there was a notable difference in the displacement between the joint baseplate and the H-shaped steel attributable primarily to the L-shaped connectors' thickness. When joint M-SWMC-J-2 was compared with joint M-SWMC-S-2, it was found that when the impact was at the joint, cracks appeared on the wooden column's upper part and sides. However, when the impact was at the steel column's mid-span, there was almost no significant deformation in the wooden column, indicating that the impact's location has a significant effect on the wooden column's deformation.

For the joint M-SWMC-W, the impact's location was changed again. As can be seen in Fig. 19, when the impact was on the wooden column, depression in the span of a wooden post, plastic hinges form rapidly in depressions and extend along the length of the wood post, and cracks appeared in the direction of the length of the extended wood columns, deformation of the L-shaped connector appeared, and displacement of the bottom plate of the node and the upper end of the H-beam columns appeared. After the third impact, the deformation of the L-shaped connector increased dramatically, the plastic hinge region was further extended, and the depth of the depression and the extent of the damage at the impact of the wooden column were significantly enlarged. When the impact location in the wood column, it not only had a significant effect on the joint's L-shaped connectors, but also caused significant damage to the wooden column itself. Similarly, because the L-shaped connectors were weak, significant deformation occurred at the connection between the steel column and the joint.

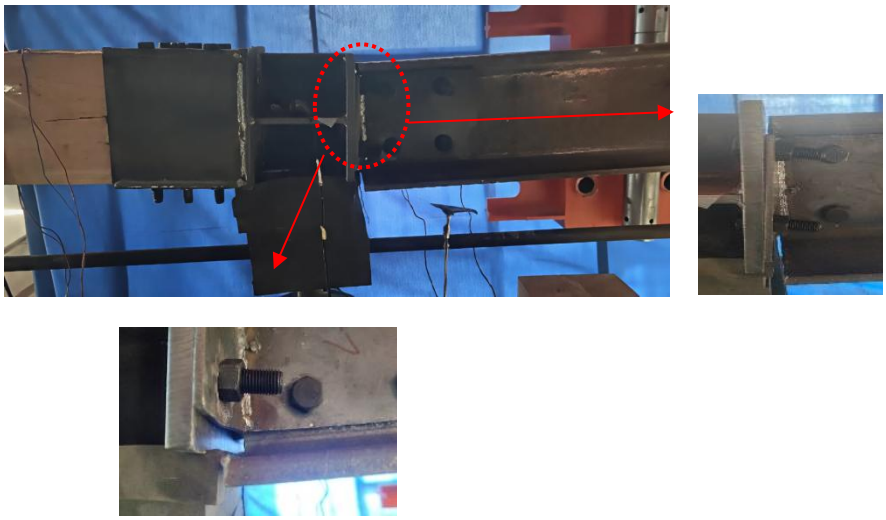

Fig. 14 Deformation mode of specimen M-SWMC-S-1 after impact

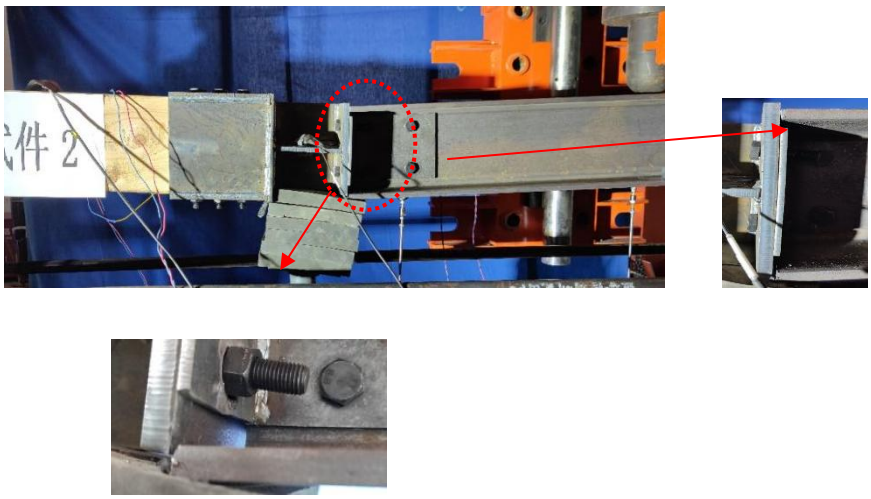

Fig. 15 Deformation mode of specimen M-SWMC-S-2 after impact

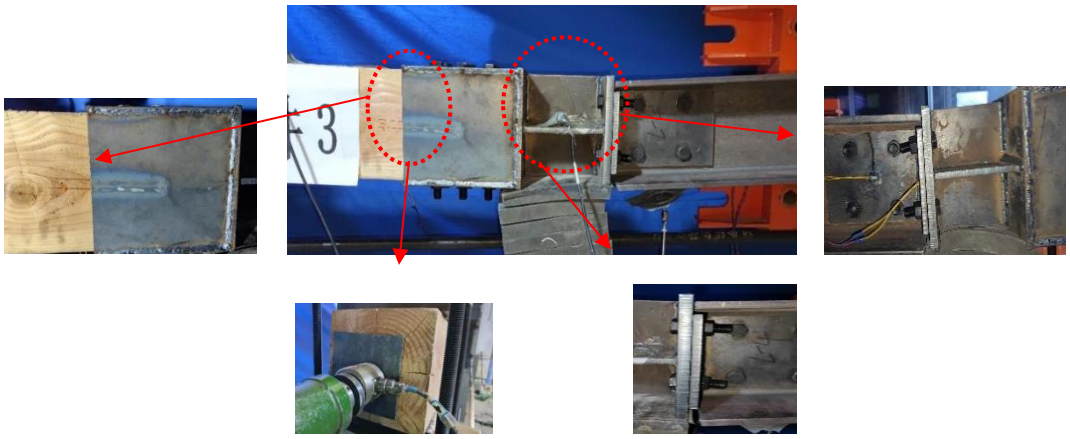

Fig. 16 Deformation mode of specimen M-SWMC-S-3 after impact

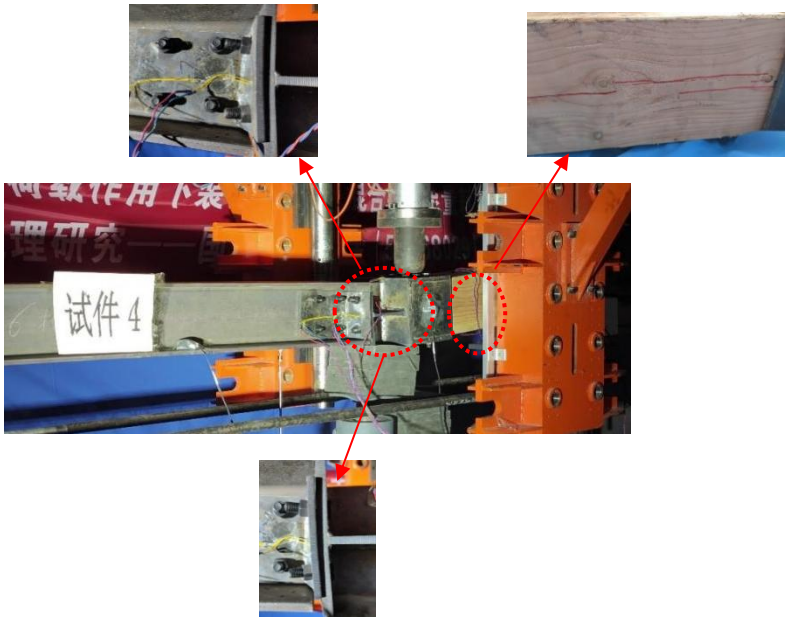

Fig. 17 Deformation mode of specimen M-SWMC-J-1 after impact

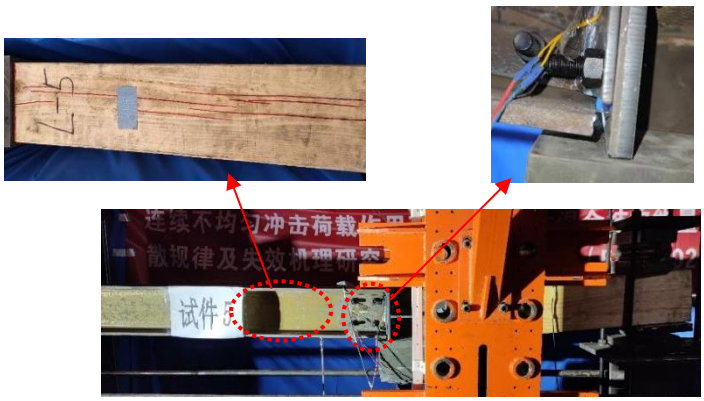

Fig.18 Deformation mode of specimen M-SWMC-J-2 after impact

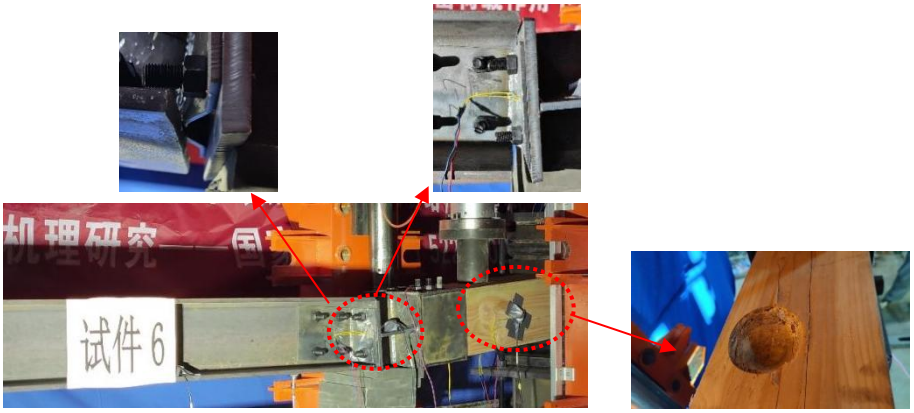

Fig. 19 Deformation mode of specimen M-SWMC-W after impact

4. Test results

4.1. Time history curves of impact force

Fig. 20(a)-(c) illustrates the M-SWMC-S-1-3 specimen's impact force-time course curves under three consecutive impacts. A detailed analysis of these impacts' effects on the M-SWMC-S-1 specimen revealed that, because of the hammer's lower height, the first impact placed the specimen in the elastic stage, which resulted in an impact force-time history curve that differed from the subsequent two impacts. The latter two exhibited similar trends, with peak impact forces of 91.8 kN, 433.3 kN, and 475.5 kN, respectively. The smaller peak impact forces of 190 kN and 215 kN during the second and third impacts indicated that consecutive impacts do not alter the impact forces' development pattern. The duration of the three consecutive impacts increased progressively (from 0.0233s to 0.0318s), which suggests that the impact energy intensifies with increasing velocity, and thereby prolongs the time for the impact's force to decay to zero. The accumulation of residual deformation under multiple impacts did not affect the dynamic changes in the single-impact force significantly. For M-SWMC-S-2, the results showed that the development trend of impact forces under three consecutive impacts also conformed to the pattern aforementioned. In the case of M-SWMC-S-3 under three impacts, the peak values were 276.9 kN, 468.7 kN, and 522.2 kN, respectively. Notably, the difference between the second and third peak values was significantly smaller than that between the first and second, which can be attributed to the cumulative damage from the first two impacts, which caused the weak points in the component to yield, and thereby limited the further surge in impact force and stabilized the peak values. The maximum impact force is shown in Fig. 21.

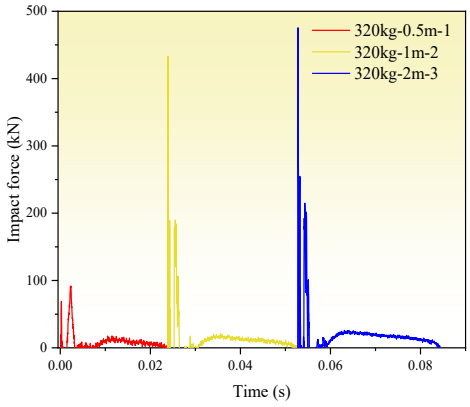

(a) M-SWMC-S-1

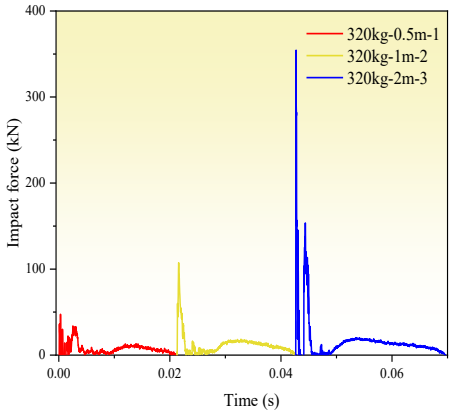

(b) M-SWMC-S-2

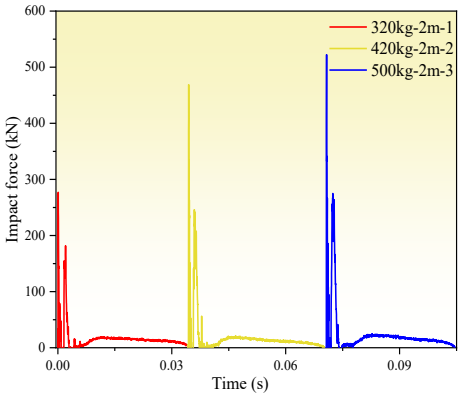

(c) M-SWMC-S-3

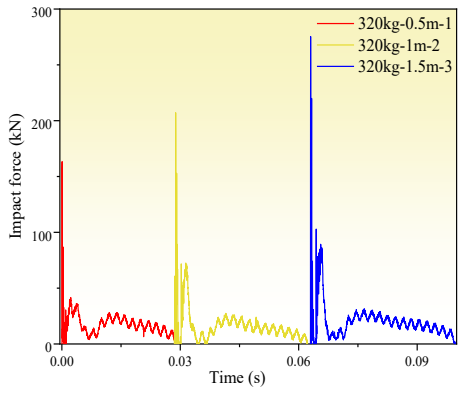

(d) M-SWMC-J-1

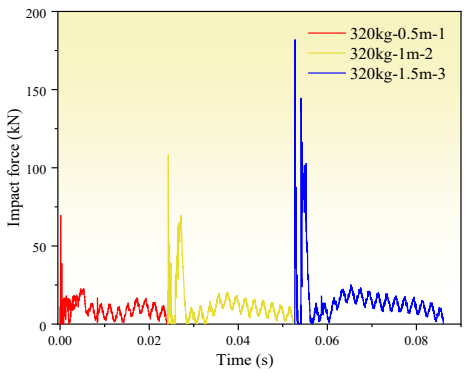

(e) M-SWMC-J-2

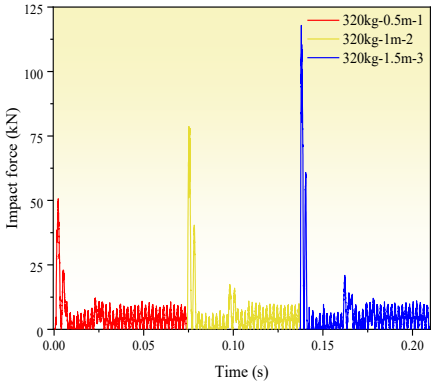

(f) M-SWMC-W

Fig. 20 Impact force-time course curve of specimen 1-6

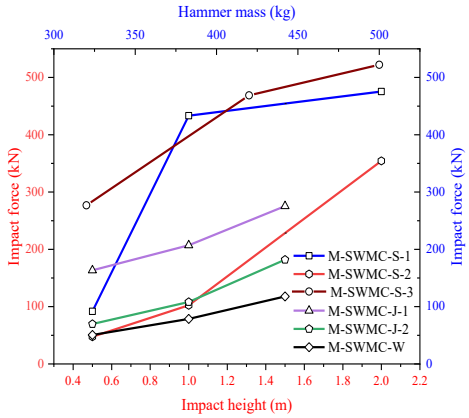

Fig. 21 Maximum impact force of specimen 1-6

Fig. 20(d)-(f) shows the time-history curves of the impact force for specimens M-SWMC-J-1-2 and M-SWMC-W. A detailed analysis of the results of three consecutive impacts on specimens M-SWMC-J-1 and M-SWMC-J-2 revealed that the two specimens' impact force trends were similar. However, because the L-shaped connectors were thicker, M-SWMC-J-1's peak force was higher than that of M-SWMC-J-2, and provided the joint with greater strength. The abnormally high peak impact force in M-SWMC-J-2's second impact is attributable to the larger vertical displacement caused by its L-shaped connectors' weakness, which enhanced the spring support's reaction force and affected the peak impact force subsequently. In contrast, M-SWMC-J-1 had lower secondary peak values because of its high-strength connectors, small displacement, and weak spring reaction force.

Analysis of specimen M-SWMC-W's impact force time-history curve revealed that, because wood (specifically, soft Douglas fir) was used as the impact target, the hammer's peak impact force was significantly lower than that of the other five specimens, and reflected the wood's low strength characteristic. In addition, the impact's duration was notably prolonged. This is because the soft wood converts kinetic energy into strain energy gradually through slow deformation during the hammer and the specimen's joint movement, rather than absorbing it rapidly. Table 5 summarizes the peak impact forces and durations for all six specimens.

Table 5
Table of impact force parameters

Test piece	First impact force peak(kN)	Second Impact Peak(kN)	Third Impact Peak(kN)	Duration of first impact(s)	Second Impact Duration(s)	Duration of third impact(s)
M-SWMC-S-1	91.8	433.3	475.5	0.0233	0.0294	0.0318
M-SWMC-S-2	47.4	107.3	354.4	0.0213	0.0211	0.0269
M-SWMC-S-3	276.9	468.7	522.2	0.0343	0.0356	0.0346
M-SWMC-J-1	163.3	207.1	275.4	0.0209	0.0413	0.0367
M-SWMC-J-2	68.6	108.2	181.9	0.0241	0.0285	0.0334
M-SWMC-W	50.6	78.0	117.9	0.0740	0.0636	0.0720

4.2. Time history curves of displacement

Fig. 22 displays the six specimens' vertical displacement time-history curves under three impacts, and shows that they exhibited similar trends: after the initial impact, the displacement increased and then decreased. This phase involved the hammer and the specimen's joint downward movement, followed by a rebound. The specimen continued to move upwards because of the spring support's reaction force, and exceeded its initial position eventually, which manifested as a negative valley value in the displacement curve. Subsequently, the peak displacement results from the superposition of the hammer's secondary fall and the specimen's downward movement. The final stable displacement is attributable to residual deformation. This indicates that the impact's energy has a significant influence on the specimens' residual deformation. Taking specimen M-SWMC-S-1 as an example, after three consecutive impacts with a 320kg hammer at a height of 0.5m, its deformation remained within the elastoplastic range. The residual deformation after a single impact was not significant, with a cumulative residual deformation of 27.5mm after three impacts, which increased to 6.6mm, 9.1mm, and 11.8mm, respectively, after each impact. In contrast, specimen M-SWMC-S-2 exhibited different deformation characteristics under the same conditions: the residual deformation after the first impact was 6.4mm,

with almost no increase after the second impact, indicating that the spring support mitigated deformation effectively. However, the third impact increased the deformation significantly to 10.2mm, and resulted in a cumulative deformation of 23.1mm. Notably, during the second fall of the hammer, the displacement surges, reflecting that the increased velocity prompted the specimen to dissipate more energy through plastic deformation. Because of the combined increase in the hammer's velocity and mass, specimen M-SWMC-S-3 had a significantly enhanced impact force and support reaction force, which led to the specimen's increased negative displacement. The final residual deformation reached 21.0mm, further confirming that the impact's energy had a pronounced effect on the specimen's residual deformation. The maximum displacement is shown in Fig. 23.

For specimen M-SWMC-J-1, the impact tests at the joint revealed that as the hammer's height increased, the impact's peak force rose gradually (25.2mm, 34.8mm, 44.4mm). The residual deformation also accumulated progressively, with 4.8mm after the first impact, increasing to 7.4mm after the second, and reaching 15.7mm after the third, resulting in a total residual deformation of 27.9mm. Although M-SWMC-J-2 exhibited a similar displacement trend, compared to M-SWMC-J-1, the residual deformation was reversed. After the first impact, the residual deformation was significant (15.2mm), and then decreased to 11.1mm and 7.4mm, with a cumulative total of 33.7mm. This phenomenon is attributable to its thinner L-shaped connectors, which formed plastic hinges under joint impacts quickly, absorbed energy effectively, and strengthened as the number of impacts increased, thereby limiting subsequent displacements. Specimen M-SWMC-W's residual deformation behavior was similar to that of M-SWMC-J-2, with values of 19.9mm, 12.3mm, and 5.4mm in sequence, and a cumulative total of 37.6mm. Similar to M-SWMC-J-2, the significant formation of plastic hinges in the L-shaped connectors after the first impact inhibited the displacement response to subsequent impacts significantly.

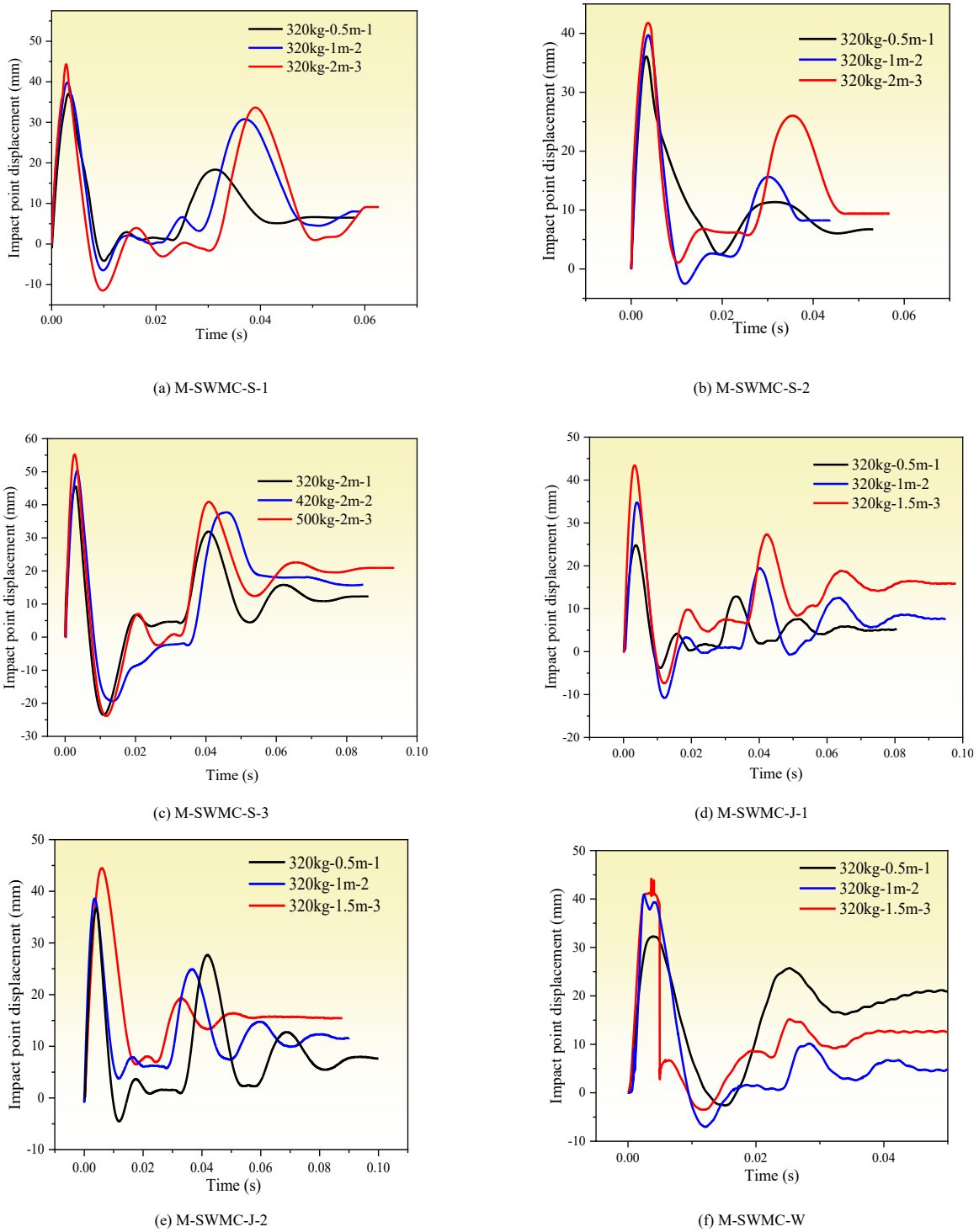

(a) M-SWMC-S-1

(b) M-SWMC-S-2

(c) M-SWMC-S-3

(d) M-SWMC-J-1

(e) M-SWMC-J-2

(f) M-SWMC-W

Fig. 22 Displacement time curve of specimens 1-6

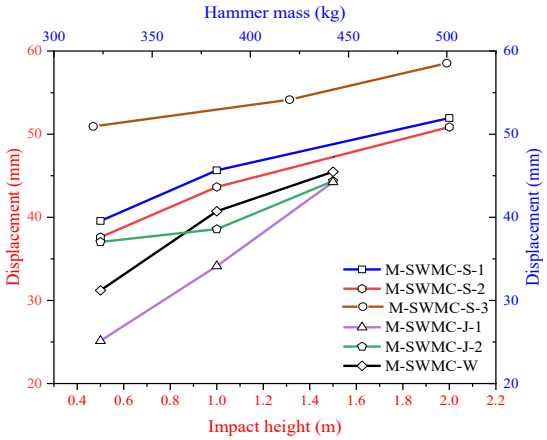

Fig. 23 Specimens 1-6 of maximum displacement

4.3. Time history curves of acceleration

In this experiment, accelerometers were installed at three locations on specimen 1, and we analyzed the acceleration changes by taking M-SWMC-S-1 as an example. Fig. 24(a)-(d) shows that during the second impact, the peak acceleration reached 7861m/s² at the impact's location and 5240m/s² at the joint. During the third impact, these values increased to 8294m/s² and 7840m/s², respectively.

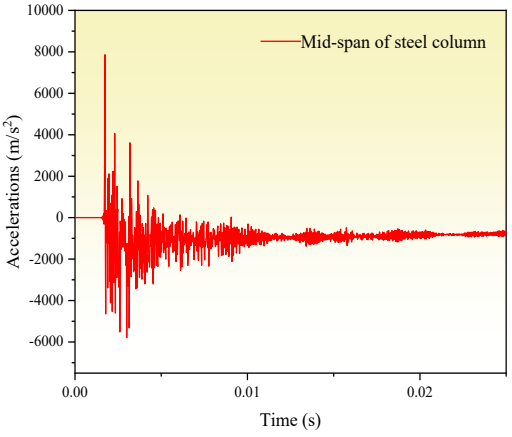

(a) M-SWMC-S-1 second impact mid-span of steel column acceleration

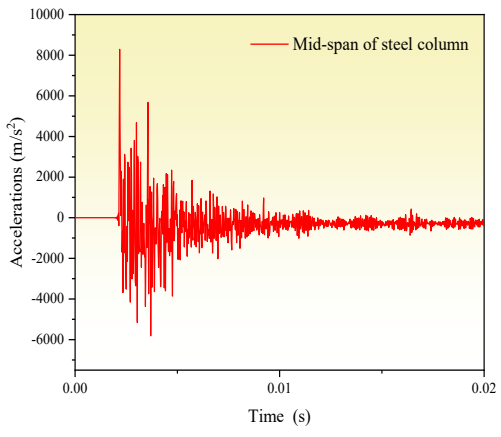

(b) M-SWMC-S-1 third impact mid-span of steel column acceleration

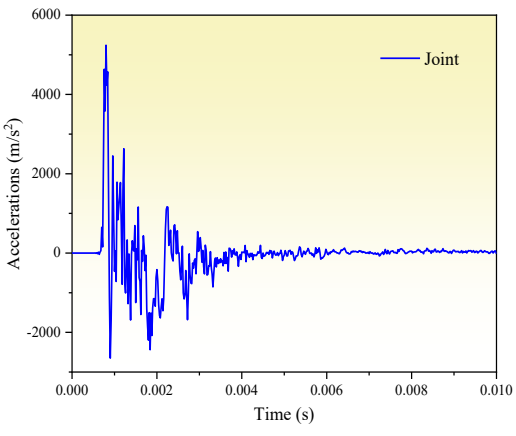

(c) M-SWMC-S-1 acceleration at second impact joint

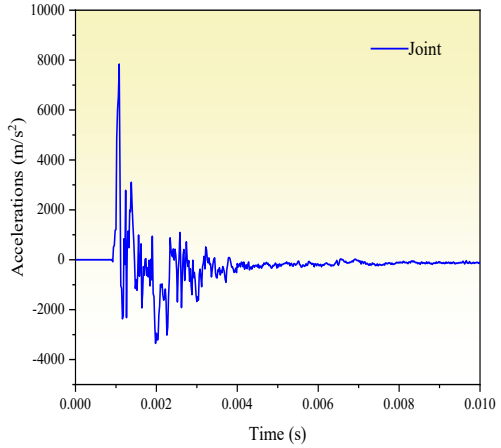

(d) M-SWMC-S-1 acceleration at third impact joint

Fig. 24 Acceleration time-course curve of specimen 1

5. Numerical simulation

5.1. Constitutive relation

5.1.1. Constitutive model of steel

During the establishment of the new joint in this paper, Q235 steel was used for the joint sleeve, L-shaped connectors, steel columns, steel beams, and joint-to-beam connectors, and grade 8.8 M16 bolts were used for bolts. Under the action of impact load, the joint was in a large deformation stage in the later stage, and significant deformation or even fracture may occur at the steel beam flange, web, L-shaped connector, and other locations in the joint area. Therefore, this paper adopted a metal ductile damage model and the comprehensive fracture criterion based upon stress triaxiality that Wierzbicki et al. proposed [36]. Its expression is as eq. (4).

$$\bar{\varepsilon}_d \begin{cases} \frac{\varepsilon_{d1}}{1+3\eta} & -\frac{1}{3} < \eta \le 0 \\ \varepsilon_{d1} + (\varepsilon_{d2} - \varepsilon_{d1})(3\eta)^2 & 0 < \eta \le 0 \\ \frac{\varepsilon_{d2}}{3\eta} & \frac{1}{3} < \eta \end{cases} \tag{4}$$

Where: ε_{d1} is the initial fracture strain under pure shear (η=0), and the Q235b grade steel in this paper was 0.133; ε_{d2} is the initial fracture strain under the uniaxial tensile condition (η=1/3), and the Q235b grade steel in this paper

was 0.273 [37].

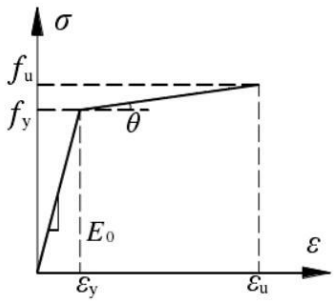

Fig. 25 Constitutive relation of steel

Table 6
Material performance parameters for strain rate effect

Density of steel (kg/m³)	Elastic modulus (GPa)	Poisson's ratio	Yield strength (MPa)	Failure strain	Ultimate strength (MPa)
7800	210	0.3	354.70	0.18	467.36

5.1.2. Constitutive model of wood

The constitutive model of wood adopts the ideal elastoplastic model that Chen proposed [38]. As shown in Fig. 26, f_{ce} represents the equivalent maximum compressive stress, and f_c represents the compressive strength, where $f_{ce} = 0.93 f_c$. denotes the maximum elastic compressive strain, ε_{ce} represents the ultimate compressive strain, ε_{tu} represents the ultimate tensile strain, and E denotes the elastic modulus of wood. The mathematical expression is given in Eq. (5).

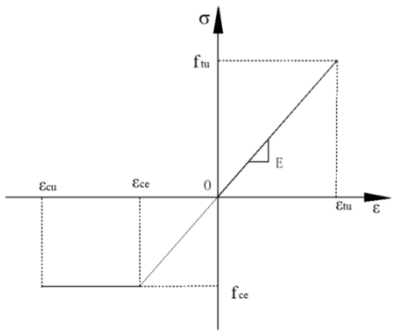

Fig. 26 Constitutive relation curve of wood

$$\sigma_w = \begin{cases} E & \varepsilon_{ce} \le \varepsilon \le \varepsilon_{tu} \\ f_{ce} & \varepsilon_{ce} \le 0 \\ f_{tu} & 0 \le \varepsilon_{tu} \end{cases} \quad (5)$$

The orthotropic materials' elastic phase analysis was conducted using the engineering constant method in Abaqus. Douglas fir wood's material properties in the model are shown in Table 7.

Table 7
Mechanical parameters of Douglas fir

E1	E2	E3	υ12	υ13	υ23	G12	G13	G23
11890	780	409	0.45	0.47	0.32	713	890	215

Note: The units of E and G are MPa; subscripts 1, 2, and 3 represent the longitudinal, radial, and tangential directions of the wood, respectively.

5.2. Model establishment

In this paper, the "surface-to-surface" contact method is utilized to construct a solid contact pair by clearly defining the master and slave surfaces of the contact according to Table 8. The "Penalty" friction formula is applied tangentially to simulate the friction force, and the coulomb coefficient of friction of the contact surfaces in the nodal model is set to 0.4 by the simple friction test of each member and the range of friction coefficients of the contact surfaces of the reference materials [39], and the coulomb coefficient of friction of the contact surfaces of the impactor and the member is set to 0.3 [40]. For the normal direction, "Hard" contact was selected, which allowed separation after contact. ABAQUS/Explicit was employed for the FEA, which is suitable for dynamic loading. Steel columns, wooden columns, steel beams, joint sleeves, L-shaped connectors, etc., were all simulated using three-dimensional solid elements with an eight-node linear hexahedral reduced integration format (C3D8R).

Table 8
Definition of contact master and slave surfaces

Different category	Surface stiffness	Mesh compactness	Area size
Contact surface	High stiffness	Thinly spread	Large area
Contact surface	Small stiffness	Compressed	Small area

5.3. Validation of finite element analysis methods

Figs. 27 and 28 compare the experimental and finite element simulation deformation modes under specimen M-SWMC-J-2's third impact load. It can be seen that both deformation modes exhibited bending deformation at the joint, separation between the H-shaped steel column and the bottom plate of the joint sleeve, and bending deformation of the L-shaped connector.

(a) Deformation pattern of specimen M-SWMC-J-2 test

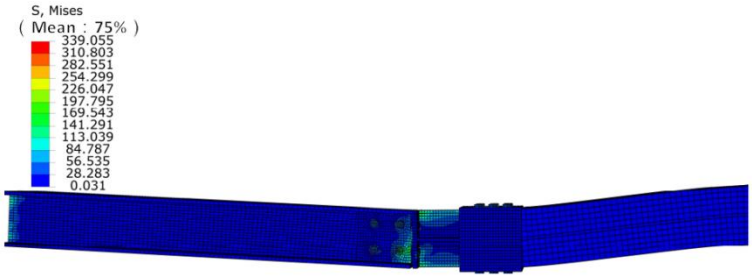

(b) Specimen M-SWMC-J-2 finite element simulation deformation mode

Fig. 27 Comparison of deformation patterns after impact for specimen M-SWMC-J-2

(a) Test L-connector deformation modes

(b) Finite element simulation of L-connector deformation modes

Fig. 28 Comparison of local deformation modes of specimen M-SWMC-J-2

Fig. 29 compares the impact force between the mid-span impact test and the finite element simulation of specimen M-SWMC-J-2 under a hammer velocity of V_0=5.477m/s and hammer mass of M=320kg. The results indicated that the impact's first peak force was 264.5kN in the simulation and 275.4kN in the experiment, with an error of only 4.1%, demonstrating high consistency before and after the peak. However, there were significant differences in the second peak and the plateau section. This is attributable to the reaction force that the spring support generated in the experiment when the specimen and the hammerhead moved upwards, which is not accounted for in the simulation. Consequently, the impact's subsequent simulated force was lower.

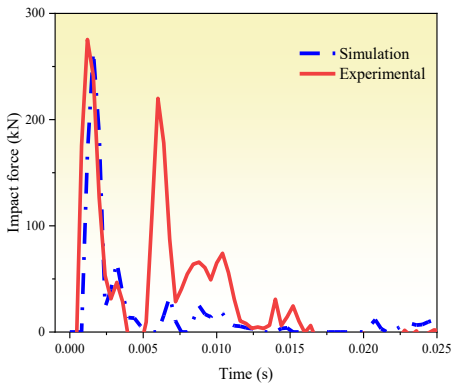

Fig. 29 Comparison of time-range curves of impact force for specimen M-SWMC-J-2

5.4. Destruction mechanisms

5.4.1. Nodal deformation patterns

Summarizing the joint's deformation characteristics at three impact locations, it was found that the steel column and the wooden column exhibited different deformation modes because their material properties differed. Steel columns, due to high modulus of elasticity and ductility, are mainly subject to local buckling or bending deformation under impact, and plastic deformation is concentrated in the joint connections, which maintains better overall integrity; wood columns, as anisotropic materials, are prone to brittle cracking or out-of-plane instability near the point of impact under impact, accompanied by fiber tearing or cross-grain cracking. At lower impact energies, changes in the impact's location had a limited effect on the joint overall, which manifested primarily as local deformation at the point of impact. This is because of the instantaneous nature of the impact process, where the energy fails to diffuse rapidly throughout the entire specimen, and the stress wave does not propagate to the other end of the impact's location, which causes significant deformation to occur locally (particularly in weak areas), and triggers out-of-plane instability. However, this local deformation dissipates most of the impact's energy effectively, which limits the propagation of stress to other parts, and keeps most specimen areas in an elastic state, while plastic deformation is concentrated at the joints and connections. Specifically, the displacement between the H-shaped steel and the bottom of the joint sleeve is caused by the L-shaped connector's tension and bending. Fig. 30 shows the structural plastic strain and stress programs under different impact locations. The quantitative comparison shows that steel absorbs energy through localized plastic deformation due to its ductility, while wood components dissipate energy through localized cracking due to their brittle characteristics. Quantitative comparisons show that steel absorbs energy through localized plastic deformation by virtue of material ductility, while wood components dissipate energy through localized cracking due to their brittle characteristics, and that the energy absorption mechanisms of the two are significantly different due to differences in material properties.

5.4.2. Damage evolution

Under an impact energy of V_0=7m/s and M=500kg, specimen M-SWMC-S-2's damage evolution (taking the steel's mid-span impact as an example) can be explained through the equivalent plastic strain. Fig. 31 shows that at the impact's peak force, stress waves propagated from the impact location to the joint, which caused minor plastic damage initially at the connection between the joint and the beam. As the impact process progressed, the stress waves were transmitted toward the beam ends and the ends of the wooden column, and the damage also extended along the specimen's joint toward both ends of the steel beam and the connections between the wooden column and the joint. During the plateau phase of the impact's force, the damage concentrated in the steel column's mid-span impact zone, the connections between the steel beam and the joint, as well as the connections between the wooden column and the joint, with significant aggravation of bending deformation at the joint. By the end of the plateau phase, the specimen's deformation reached its limit, and the damage accumulated to its maximum value and no longer increased. The L-shaped connector bent under tension, displacement occurred at the connection between the joint and the steel column, and the steel beam and joint connector were compressed and deformed. In the attenuation stage of the impact's force, although there was some rebound in the bending of the joint overall, the equivalent plastic strain remained relatively stable until the end of the impact.

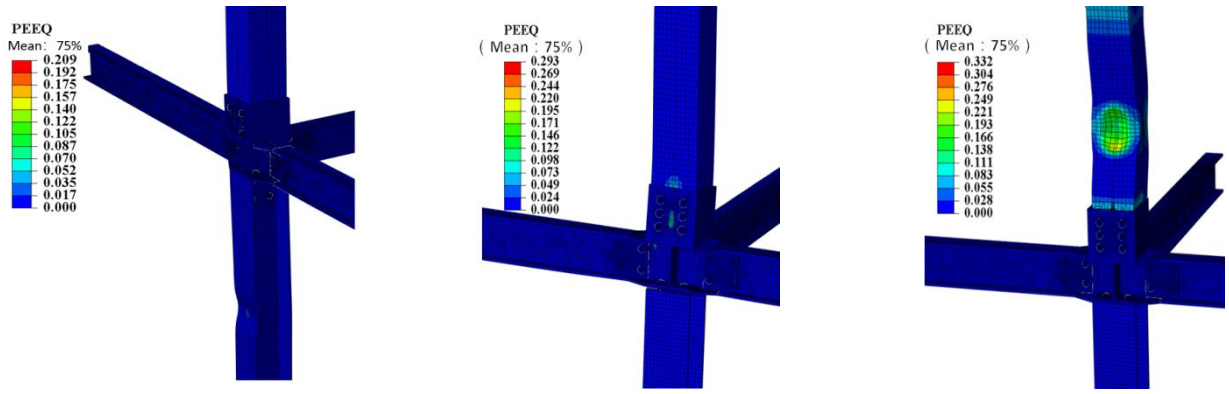

(a) Plastic strain in the span of impact steel

(b) Plastic strain at impact joint

(c) Plastic strain at impact on a wooden column

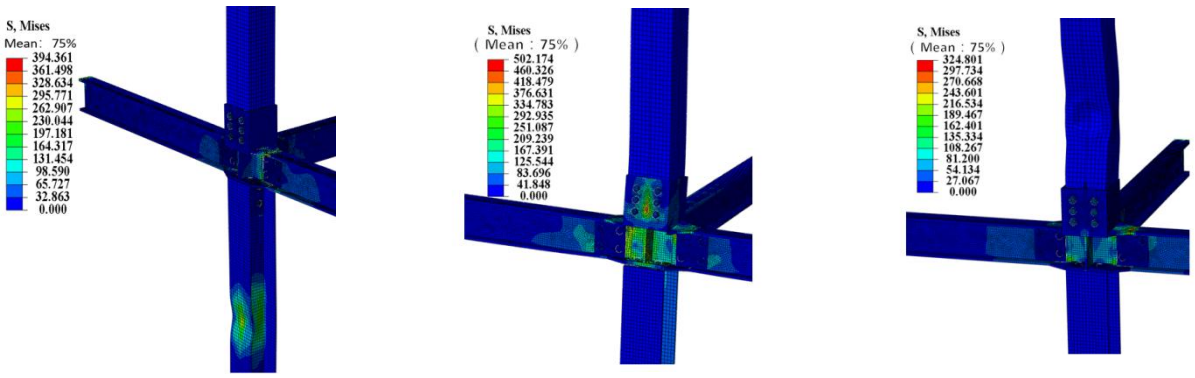

(e) Impact steel span-time stress cloud (f) Stress cloud at impact joint (g) Stress cloud at the time of impact on a wooden post

Fig. 30 Joint deformation pattern under impact loading

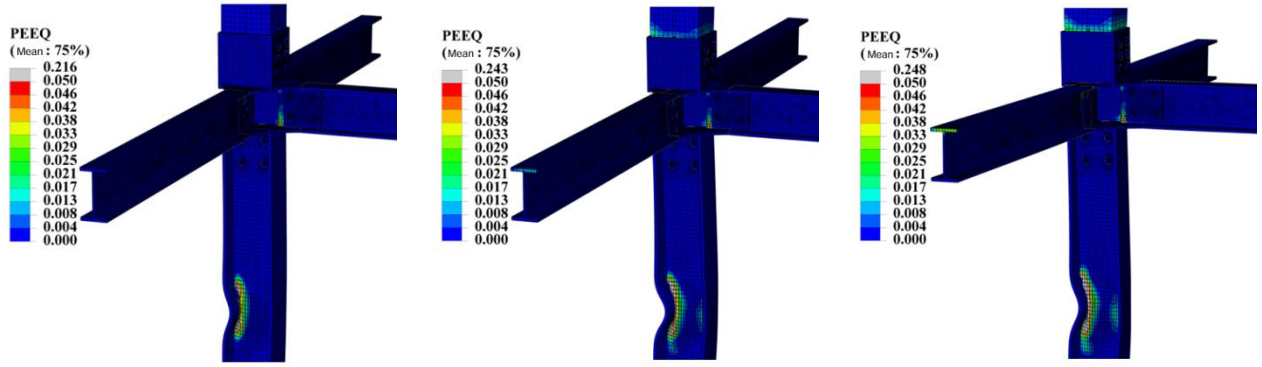

(a) At peak impact force (b) At the impact platform stage (c) When deformation reaches its maximum

Fig. 31 Joint's equivalent plastic strain development when the impact location is in the steel span

6. Parametric study

6.1. Different hammer masses

The dynamic response of joint M-SWMC-S-2 increases with increasing impact mass when the impact velocity V_0=7m/s (Fig. 32). The maximum displacements and maximum impact forces at the joints for different hammer masses are shown in Fig. 33. When the hammer mass increases from 320 kg to 700 kg, According to the conservation of momentum, the initial momentum of the impactor interacts with the specimen to produce an increased impulse, the joint displacement increased with the hammer's mass and reached a maximum of 240mm at 700kg without convergence in the displacement curve, indicating the column's failure overall. The increase in the impact force plateau value, displacement, and impact duration is consistent with the impulse theory, i.e., the increase in mass prolongs the time of action between the impactor and the specimen, which allows for a more adequate transfer of energy and leads to an expansion of the deformation region.

Deformation patterns of H-beam columns demonstrate the relationship between energy absorption and material plasticity development. At a hammer mass of 320 kg, the small impact momentum causes only a slight local deformation. The energy is mainly absorbed by the elasticity of the steel column; with the increase of mass, the impulse increases to promote the transfer of stress waves to the joints, and the plastic deformation gradually extends from the impact point to the joints and beam ends. When the mass reaches 700kg, the L-connector is damaged in tension and bending due to the excessive impulse, leading to the failure of the structure as a whole. It is worth noting that the increase in the peak impact force is not significant. This is because the development of impact force in the early stage is mainly limited by the impact velocity, while the effect of mass increase is more concentrated in the later stage of stabilization and decay, reflecting the stage-by-stage mechanism of the impulse-momentum relationship in the process of dynamic response.

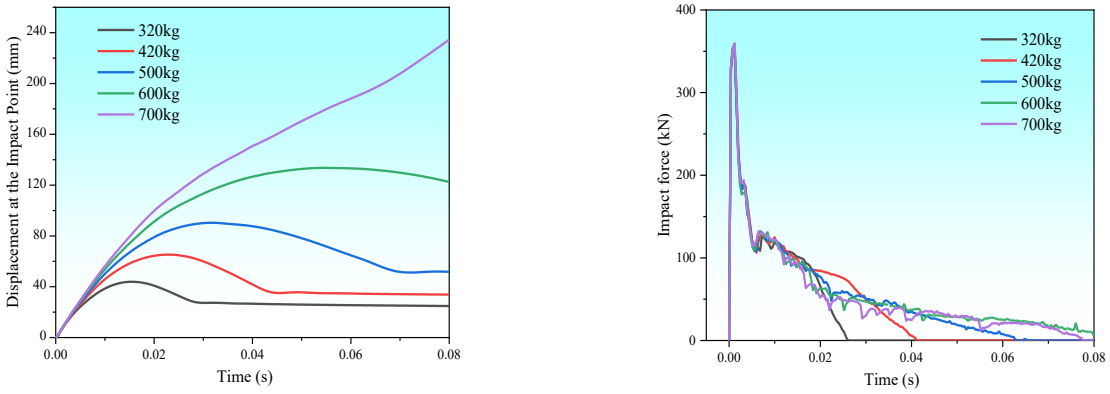

(a) Vertical displacement time course Curve (b) Impact force time course Curve

Fig. 32 Dynamic response of the joint under different hammer masses

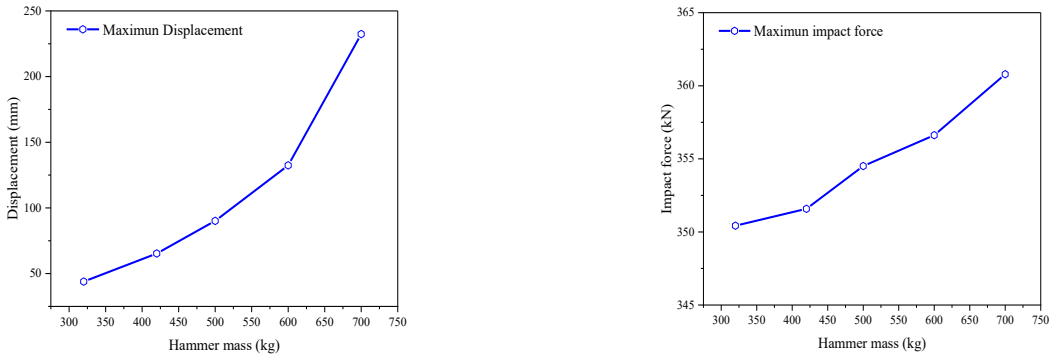

(a) Maximum displacement (b) Maximum impact force

Fig. 33 The maximum displacements and maximum impact forces at the joints for different hammer masses

6.2. Different hammer velocities

The dynamic response of the joint M-SWMC-S-2 shows a regular variation with the increase of the impact velocity V_0 at the falling hammer mass M = 320 kg (Fig. 34). The maximum displacements and maximum impact forces at the joints for different hammer velocities are shown in Fig. 35. The increase in impact velocity increases the initial momentum of the impactor, and according to the momentum theorem, the impulse generated when interacting with the specimen also increases, resulting in a significant increase in the peak impact force, plateau value and displacement of the impact point. When V_0 was less than or equal to 7m/s, because of the small initial momentum and the short duration of the shock action, the impact force plateau was not evident. However, at V_0=10m/s, a significant increase in the momentum of the impactor and prolongation of the interaction time with the specimen, a significant impact force plateau, and the impact's duration was extended greatly. When V_0 was greater than or equal to 7m/s, the displacement at the impact point increased steadily with increasing velocity. The member is in the elastic phase because the impulse transmitted by the impactor does not exceed the limit of absorption of the elastic deformation energy of the material. At V_0=10m/s, excessive initial momentum that causes the impulse to exceed the elastic limit of the material by a wide margin, causes the member to enter an elastic-plastic phase and the difference between the post-impact displacement and the maximum displacement decreases.

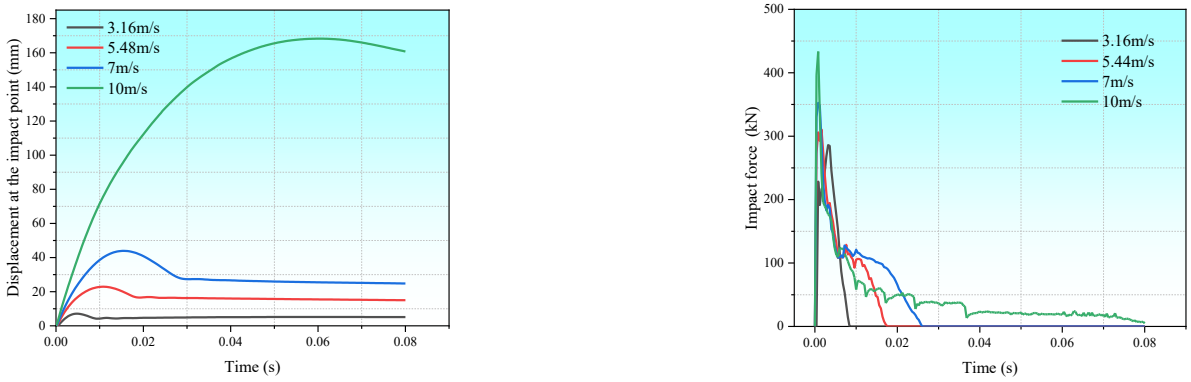

(a) Vertical displacement time history curve (b) Impact force time history curve

Fig. 34 Dynamic response of the joint under different hammer velocities

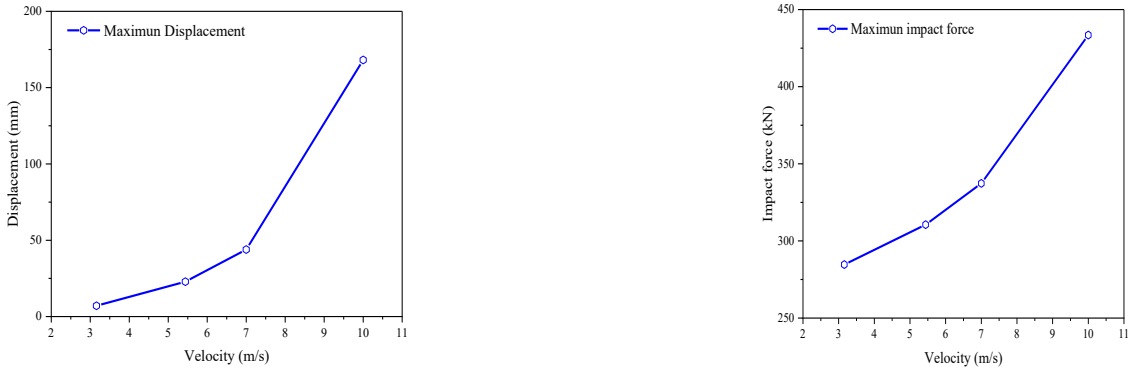

(a) Maximum displacement (b) Maximum impact force

Fig. 35 The maximum displacements and maximum impact forces at the joints for different hammer velocities

From observing the deformation patterns: At V_0=3.16m/s, deformation occurred at the H-shaped steel column's flange at the impact site, with no plastic deformation at the joint. As the velocity increases, the impulse transmitted by the impactor increases, the plastic deformation region gradually expands, and the stress wave is transmitted to the joints, resulting in displacements of the beam ends, the L-shaped connectors, and the base plate. At V_0=10m/s, the significant deformation of the steel column span due to excessive impulse, which formed a plastic hinge between the baseplate and the L-shaped connector. The bolt holes were enlarged, and displacement arose between the connecting plate and the beam. The connection edge between the wood column and the joint sleeve pulled apart, resulting in the joint's severe deformation overall.

6.3. Different impact locations

Under the condition of a falling hammer mass M=320kg, impact velocity V_0=7m/s (i.e., constant initial momentum), taking joint M-SWMC-S-2 as an example, the impacts of different impact positions on the joint are different due to different impulse transmission paths and material properties. When impacting the steel column span and node, because both materials are steel, the stress wave propagation characteristics are similar, so the displacement and impact force curves are similar in shape (Fig. 36); however, the displacement is larger when impacting the joint, this is due to the joint as the core of the structural connection, it is easy to generate displacement with the steel column connection, and it is easier to trigger deformation of the connection during the transfer of the impulse, which results in the accumulation of the displacement. Wooden columns are more susceptible to denting upon impact due to the low modulus of elasticity of the material and weak plastic deformation capacity. The low efficiency of impulse transfer leads to longer impact action time, longer duration of the impact force platform, and because the wood itself absorbs a large amount of energy, it is difficult for the stress wave to be transmitted to the joints and steel columns to keep them in an elastic state. The maximum displacement and maximum impact force of the joints at different impact locations are shown in Fig. 37.

From the deformation mode, when impacting the steel column span and joint, the impulse causes the L-shaped to be tensile and bending, triggering the displacement of the joint base plate and the steel column, and when impacting the joint because it is closer to the connectors, the impulse transfer is more direct, and the displacement response is more significant; When impacting wooden columns, the plastic deformation (depression) and elastic deformation (cracks on the bottom surface of the connection edges and voids in the upper part) of the wood effectively dissipate the impulse, limiting the propagation of the stress wave to the nodes and the steel columns, thus avoiding deformation of the latter two.

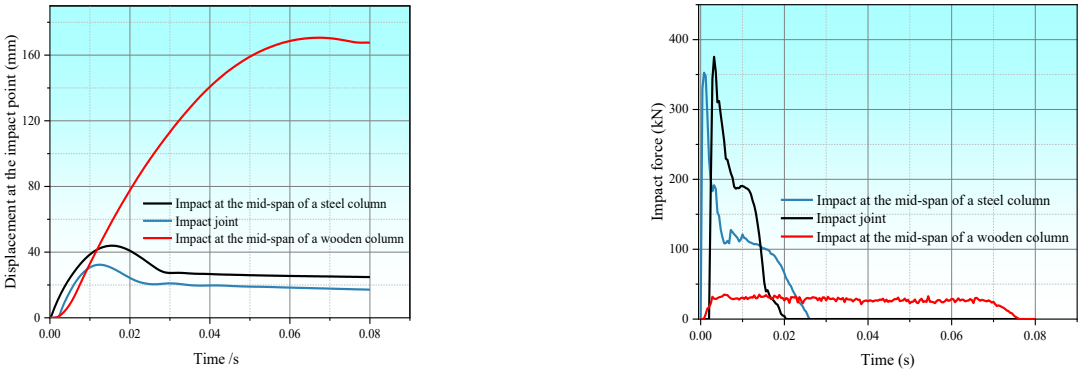

(a) Vertical displacement time history curve

(b) Impact force time history curve

Fig. 36 Dynamic response of the joint at different impact locations

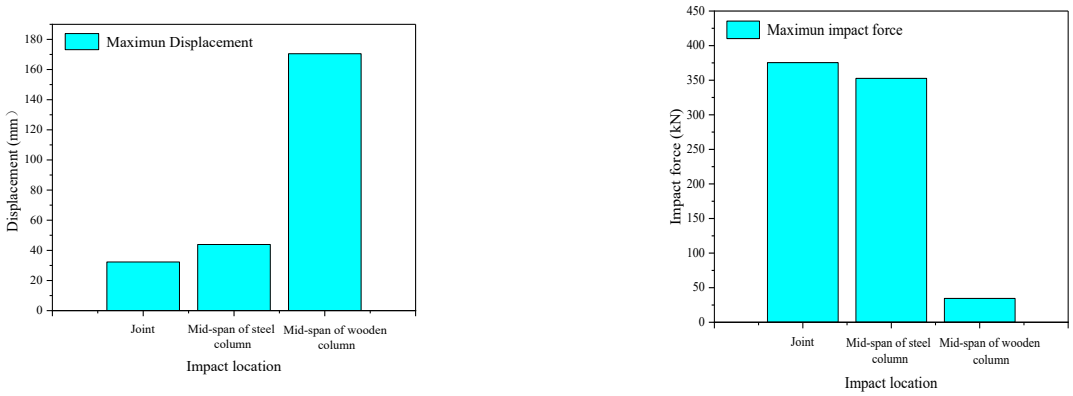

(a) Maximum displacement

(b) Maximum impact force

Fig. 37 The peak displacements and peak impact forces at the joints for different impact locations

7. Conclusion

This paper conducted experiments and finite element simulations that focused on the new prefabricated steel-wood hybrid columns, and investigated their performance in resisting impact. The conclusions drawn from the study are as follows:

(1) The hammer impact test reveals that the key deformation characteristic of the new steel-wood hybrid beam-column joint is the bending deformation at the joint, which in turn triggers the bending of the overall member. By adjusting the impact location, the weakest link in the structure was found to be the connection area between the L-shaped connector and the wooden column at the joint. Further experiments showed that increasing the L-shaped connector's thickness reduced its deformation under the same impact energy and mitigated the column's bending overall effectively. Combining the results of the comparative tests, the optimum parameters were determined to be: sleeve thickness of 5mm and L-shaped connector thickness of 10mm. Therefore, the actual design should focus on strengthening the strength of the L-shaped connector to ensure that the joints will not be damaged before the members, so as to improve the impact resistance of the overall structure.

(2) The drop weight impact test and the joint's finite element simulation showed that, when the component's impact resistance under three impact locations was compared, the dynamic response and deformation mode were similar when the steel column and the joint sustained impact. In contrast, the damage to the wooden column itself was significantly greater than the former

two when the column sustained impact. Therefore, it is recommended that special attention be paid to the wood's force transmission mechanism in the design of steel-wood hybrid structures.

(3) Upon analyzing the experimental and simulation data, it was found that an increase in the hammer's velocity enhanced the impact's peak force and extended the impact plateau significantly, indicating that the hammer's velocity is a crucial influencing factor. On the other hand, an increase in the hammer's mass extended the impact's force decay time primarily, and had a limited influence on the peak value, suggesting that the impact attributable to the hammer's mass is concentrated in the later stages of the impact.

(4) The structure dissipated impact energy primarily through the component's plastic strain energy and the L-shaped connector under impact. As the wooden column's capacity to dissipate energy was much lower than that of other parts of the hybrid column, the situation in which the wooden column fails before the component under impact should be considered fully during design.

Acknowledgments

This work is supported by the National Natural Science Foundation of Chi na (Grant No.52268029)and the Open Fund of Shock and Vibration of Enginee ring Materials and Structures Key Laboratory of Sichuan Province (Grant No .20kfgk03).

Authorship contribution statement

Chang Wu: Conceptualization, Data curation, Methodology, Software, Visualization, Writing - original draft, Writing - review & editing.

Yingni Fan: Investigation, Writing - review & editing, Software, Validation, Supervision.

Yuehan Zhang: Writing - review & editing, Validation.

Yutong Tian: Software, Investigation, Methodology.

Conflict of interest statement

We declare that we have no financial or personal relationships with others or organizations that can inappropriately influence our work.

References

[1] Gou B. L., Wang X. L., Wu C. (2023). Experimental and numerical study on the behavior of single-layer spherical reticulated shells under the combined action of temperature and impact load, Thin-Walled Structures, 182: 110333.

[2] Fábio C., Isabel V., João A., Eduardo A. (2024). Experimental characterization of bond between concrete and HDG steel tubes for mixed steel-concrete structures. Materials and Structures, 57.

[3] Xu F., Yuan Z., Liu N., Li Z. X., Jia L. G., Xu W. (2023). An experimental study on seismic performance of steel composite beam-column regid joint and buckling restrained knee-braced. Advanced steel construction, 19(4): 375-382.

[4] Feng J., Jin J., Xia J., Fang Y. Z. (2021). Experimental study on seismic performance of PEC composite column-steel beam frame with welded T-stub strengthened connections. Advanced steel construction, 44974-981.

[5] Du Y. F., Li F. Y., Li H., Hong N. (2024). Seismic behavior and resilience assessment of prefabricated beam-column joint with replaceable graded-yielding energy-dissipating connectors. Engineering Structures, 319, 118814-118814.

[6] Zhang C. W., Gholipour G., Mousavi A. (2019). Nonlinear dynamic behavior of simply-supported RC beams subjected to combined impact-blast loading. Engineering Structures, 181: 124-142.

[7] Damian K., Aleksander K., Bartosz M., Dominika Z. (2024). Experimental investigation of steel beam-to-column end-plate joints under static and impact loading. Journal of Constructional Steel Research, 212.

[8] Chen K., Zhao Y., Tan K. H. (2021). Behaviour of steel beam-column joints subjected to quasi-static and impact loads. Journal of Constructional Steel Research, 183.

[9] Deng P., Chang D. S., Chen X. L., ;Zhu Z. Y., Raheel A. (2024). Analysis of the dynamic mechanism of square tubular T-joints with chord flanges subjected to impact loading. Advanced steel construction. 19(4): 375-382.

[10] Zeng L., Liu Y. H., Zhang H., Liu C. J. (2022). Experimental study on dynamic response and residual mechanical behavior of SRC columns under repeated lateral impacts. Engineering Failure Analysis, 138.

[11] Wei J. H., Xue J. Y., Hu Z. B., Qi L. J.(2024). Experimental study on dynamic shear-behavior of H-shaped SRC columns under lateral impact loading. Journal of Constructional Steel Research,213: 108396-.

[12] Zhu X., Kang M., Fei Y. F., Zhang Q. (2021). Impact behavior of concrete-filled steel tube with cruciform reinforcing steel under lateral impact load. Engineering Structures,247.

[13] Kang X. J., Liu Y. H., Zhao L., Yu Z. X., Zhao S. C., Tang H. (2019). Dynamic response analysis method for the peak value stage of concrete-filled steel tube beams under lateral impact. Advanced steel construction. 15(4): 329-337.

[14] Huang Z. J., Cek S., Chen W. S., Paing M., Li D. Q., Hao H.(2025). Impact performance of fibre reinforced geopolymer concrete beams with steel-FRP composite bars, Engineering Structures, 329: 119880-119880.

[15] Huang J. Z., Fu C. J., Yu Z. Q., Huang Y. T., Cai H. M., Chen H. Y., Luo C. S. (2024). Impact resistance performance and simplified calculation method of web-opened steel beams under impact loads, Journal of Constructional Steel Research, 218: 108688-.

[16] Zhu B. R., ZhangY. H., Ye H. Z., Wei Y., Pan J. L., Zhang M. Z.(2025). Low-velocity impact performance of biomimetic 3D printed engineered cementitious composites beams, Construction and Building Materials, 470: 140550.

[17] Zou D. L., Teng J.L., Xu L. (2024). Exploring the impact resistance performance of RC beams based on an enhanced interpretable automated machine learning approach, Structures, 70: 107893-107893.

[18] Zhu Y., Liu Q. G., Zhang X. Y., Xing Z. Q., Zhang W. P., Chen Y., Wang L. (2025). Experimental and numerical investigations of UHPFRC beams under impact loading, Structures, 74: 108360.

[19] Wu Q. J., Zhi X. D., Guo M. H. (2019). Finite element analysis for the progressive failure of FRP-reinforced steel component under low-velocity impact. Advanced steel construction, 15(3): 267-273.

[20] Yang R. Y., Wan J., Zhang X. F. (2021). Modelling of steel-timber composite beams: validation of finite element model and parametric study. Wood Research, 66:5.

[21] Xu L., Navid K., Li M. Z. (2021). Design improvement of a composite-to-steel butt-joint based on finite element analysis. Ocean Engineering, 238.

[22] Kia L., Valipour H. R. (2021). Composite timber-steel encased columns subjected to concentric loading. Engineering Structures, 232.

[23] Chen Z. H., Xu J. H., Ting T.(2022). Seismic research on column base joint of L-shaped CFST columns under cyclic loading. Structures, 45: 1212-1224.

[24] Zhou T., Yang Z. X., Chen Z. H. (2022). Seismic behavior of connections between H-beams and L-shaped column composed of concrete-filled steel tube mono-columns connected by double vertical plates. Journal of Constructional Steel Research, 198.

[25] Chen Z. H., Niu X. Y., Liu J. D., Han K. S. (2021). Seismic study on an innovative fully-bolted beam-column joint in prefabricated modular steel buildings. Engineering Structures, 234.

[26] Chen F., He M. J., Li M. H., Liu J. J., Shu Z. (2023). Recovery testing of self-centering steel-timber hybrid beam-column connections. Construction and Building Materials, 365.

[27] Dong H. Y., Liang X., Cao W. L. (2023). Seismic behavior of mortise–tenon joints reinforced with lightweight steel components. Journal of Building Engineering, 65.

[28] Dourado N., Silva F., Moura D. M. (2018). Fracture behavior of wood-steel dowel joints under quasi-static loading. Construction and Building Materials, 176: 14-23.

[29] Zheng L, Wang W D, Xian W. (2022). Experimental and numerical investigation on the anti-progressive collapse performance of fabricated connection with CFST column and composite beam. Engineering structures, 256.

[30] "Method for the Determination of the Moisture Content of Wood" (GB/T 1931-2009). Beijing: China Standard Press, 2009, [in Chinese].

[31] Test Method for Compression Strength Parallel to Grain of Wood" (GB/T 1935-2009). Beijing: China Standard Press, 2009, [in Chinese].

[32] "Test Method for Tensile Strength Parallel to Grain of Wood" (GB/T 1938-2009). Beijing: China Standard Press, 2009, [in Chinese].

[33] "Code for the Design of Steel Structures"(GB50017-2017). Beijing: Beijing Construction Industry Press. 2017, [in Chinese].

[34] "Handbook of Wood Construction Design", edited by the Editorial Board. Manual of wood structure design. Third edition. China Construction Industry Press.

[35] Gao L., Chang Y. D., Zhang J. F. (2023). Experimental study on buffering energy dissipation of rigid-flexible stacked protection structure of bridge abutment under rockfall impact. Journal of Vibration Engineering, 36(04): 1113-1124.

[36] Wierzbicki T., Xue L. (2005). On the effect of the third invariant of the stress deviator on ductile fracture. Cambridge, MA, USA: MIT Impact and Crashworthiness Lab.

[37] Liao F., Wang M., Tu L. (2019). Micromechanical fracture model parameter influencing factor study of structural steels and welding materials. Construction and Building Materials, 215: 898-917.

[38] Chen Y. X. Flexural analysis and design of timber strengthened with high-strength composites, [in Chinese].

[39] Wang H., Chen A. J., Yang L., Li S. L., He G. J., Wang H. L., (2023). Research on mechanical property of glued timber truss connected by steel plates and bolts, Structures, 57: 105264.

[40] Yan W., Zhang D., Zhao S. J., Zhang X., Wang Z. Q. (2025). Numerical study of low velocity impact resistance of gradient foam sandwich structures, Engineering Fracture Mechanics, 323: 111231.